Article

Geophysical Research on an Open Pit Mine for Geotechnical Planning and Future Land Reclamation: A Case Study from NW Macedonia, Greece

Nikos Andronikidis [1,*], George Kritikakis [1], Antonios Vafidis [1,*], Hamdan Hamdan [2], Zach Agioutantis [3], Chrysanthos Steiakakis [4] and Nikos Economou [1]

1   Laboratory of Applied Geophysics, School of Mineral Resource Engineering, Technical University of Crete, 73100 Chania, Greece; gkritikakis@tuc.gr (G.K.); noikonomou@tuc.gr (N.E.)
2   Petroleum Geosciences and Remote Sensing Program, Department of Applied Physics and Astronomy, University of Sharjah, Sharjah 27272, United Arab Emirates; hhamdan@sharjah.ac.ae
3   College of Engineering, Department of Mining Engineering, University of Kentucky, Lexington, KY 40506, USA; zach.agioutantis@uky.edu
4   GEOSYSTA Corporation, Kountouriotou 7 and Karaoli Dimitriou, Melissia, 15127 Athens, Greece; contact@geosysta.com
*   Correspondence: nandronikidis@tuc.gr (N.A.); avafeidis@tuc.gr (A.V.); Tel.: +30-28210-37681 (N.A.); +30-28210-37643 (A.V.)

Abstract: In open pit mining areas, knowledge of geotechnical conditions (e.g., overburden thickness, background slope, and fault locations) ensures geotechnical safety during exploitation as well as reclamation planning. The Greek Public Power Corporation initiated a research program after stability issues emerged on the southern side of the Mavropigi open pit mine in NW Macedonia. Geotechnical wells revealed steeply dipping bedrock and thin tectonic contact, indicating the need for the detailed imaging of the subsurface for future stability measures. For this purpose, a geophysical investigation aimed to extract information mostly for the dip of the interface between schist bedrock and overlaying Neogene sediments and/or limestones. Based on the high contrast of electrical properties between schists and limestones, as well as the differences in acoustic impedance and formation thickness, the seismic reflection and electrical resistivity tomography (ERT) methods were selected. The suitability of the seismic reflection for its application in this area was checked by generating synthetic seismic data, which resulted from the simulation of seismic wave propagation for geological models of the area. The acquisition parameters were determined after the noise test. Field seismic data processing produced a depth-migrated section, which revealed the existence of a fault. The use of dipole–dipole and gradient arrays, in 2D and 3D electrical resistivity measurements, ensured both the lateral and vertical mapping of schist bedrock and detected limestone bodies within the overburden. Also, the tectonic contact zone between limestone and schist formations was properly imaged. The comparison between geoelectrical and seismic sections indicated that the seismic reflection method provided a more accurate estimate of fault inclination. Finally, the geophysical survey enriched the geotechnical models necessary for sustainable mining (e.g., rational exploitation, the optimization of productivity, and zero accidents) including the planning of future reclamation.

Keywords: seismic synthetic data; seismic reflection; electrical tomography; bedrock mapping; geotechnical safety

1. Introduction

Open pit mining causes significant land use change and, apart from a negative environmental impact, it can increase the geotechnical risk, due to both the removal of the surface soils and their deposition in different areas, which are usually within the mining site. One of the main aspects of mined area reclamation is to ensure the slope stability of the areas and, thus, to increase geotechnical safety [1–3]. Even though this can increase sustainability

to a large extent, including the ecological impact at the site, the basic aspect is always safety, including the avoidance of future landslide deformations. Geotechnical surveys, which include geophysical investigations, are necessary to provide volumetric models of rock mass. The seismic reflection and the electrical resistivity tomography (ERT) methods have contributed to imaging the subsurface structure for geotechnical applications.

The shallow seismic reflection method has gained significant attention in recent decades [2–10]. Even though the seismic reflection method is commonly applied to oil and gas exploration, as well as to other relatively deep prospecting applications (more than 1 km depth), the shallow seismic reflection has been successfully utilized for coal surveys at prospecting depths less than 300 m [2,3] and for bedrock imaging [5], as well as for urban planning constructions [9]. Additionally, it has been integrated with other near-surface geophysical methods for the delineation of shallow targets, such as for imaging the near-surface sedimentary formations of hydrogeological interest at depths less than 40 m [8].

Near-surface geophysical methods in general and electrical methods in particular have been widely employed in geotechnical applications. Specifically, the electrical resistivity method (ERT) provides images of the subsurface and information regarding the variation in the rock/soil water saturation, the presence of cavities and faults, and the depth to the bedrock [11–17]. Many researchers focused their interest on the possible quantitative correlation between electrical resistivity and geotechnical parameters [18–21].

By employing the ERT method, high-resolution subsurface structural information can be obtained, offering insights into the geometry, the depth, and the paleo-relief of the bedrock, the water content, the geomechanical factors, and the composition of the sliding mass. This wealth of information plays a crucial role in studying the mechanisms contributing to slope sliding and evaluating the stability of the investigated area. Numerous studies have highlighted the significance of the ERT method in slope stability assessments [11,13,14,16,22,23].

In geotechnical investigations, many scientists have employed 3D ERT [24–27], a more efficient approach due to the 3D nature of the geological structures. To mitigate the costs associated with a full 3D survey, an alternative approach is often employed. Measurements are conducted along parallel lines. The resulting apparent resistivity data is then combined using 3D inversion techniques. This methodology provides reasonably accurate 3D geoelectric images, offering valuable insights into the subsurface resistivity distribution. Numerous studies have explored and validated the effectiveness of this approach [28–34]. While it may not capture the full complexity of a true 3D survey, it offers a cost-effective solution for obtaining valuable subsurface information in large study areas. ERT data are often processed using the RES2dinv andRES3dinv software [35,36], incorporating the relief during the inversion process.

This paper presents the results of a geophysical survey conducted next to the open pit lignite mine in Mavropigi, Kozani, Greece, to aid mainly in the assessment of slope stability for the planning of geotechnical safety during excavations and future land reclamation procedures. The latter was initiated due to the removal of soil formations, which caused extended environmental distractions. A combination of a shallow seismic reflection and the ERT methods mapped the contact between the Neogene sediments and the carbonates and/or the schists formations in three dimensions. This contact is the main surface of future landslides.

2. Study Area

The investigated area is located within the Florina, Ptolemaida, Kozani, and Sarandaporo graben systems in NW Macedonia, Greece [37]. This region belongs to the Pelagonian geotectonic zone. The basement and borders of the depression are composed of semi-crystalline to crystalline Triassic–Jurassic limestones, marbles, dolomites, and schists (Figure 1). The basin filling process began during the Late Miocene–Early Pliocene period. Various types of deposits, including terrestrial, fluvial-torrential, fluvial, lacustrine-fluvial,

lacustrine, and marshy deposits, filled the basin and contributed to the smoothing of the irregular surface of the graben basement. In the survey area near Mavropigi village, the Neogene formations are dominant and primarily consist of marls, sandy marls, and clay marls. These Neogene formations also host lignite beds, indicating the presence of coal deposits in the area. The Quaternary formations, with a thickness of a few meters, are comprised of eluvial mantles and alluvial deposits. The geological map and the survey lines of the investigated area are shown in Figure 1.
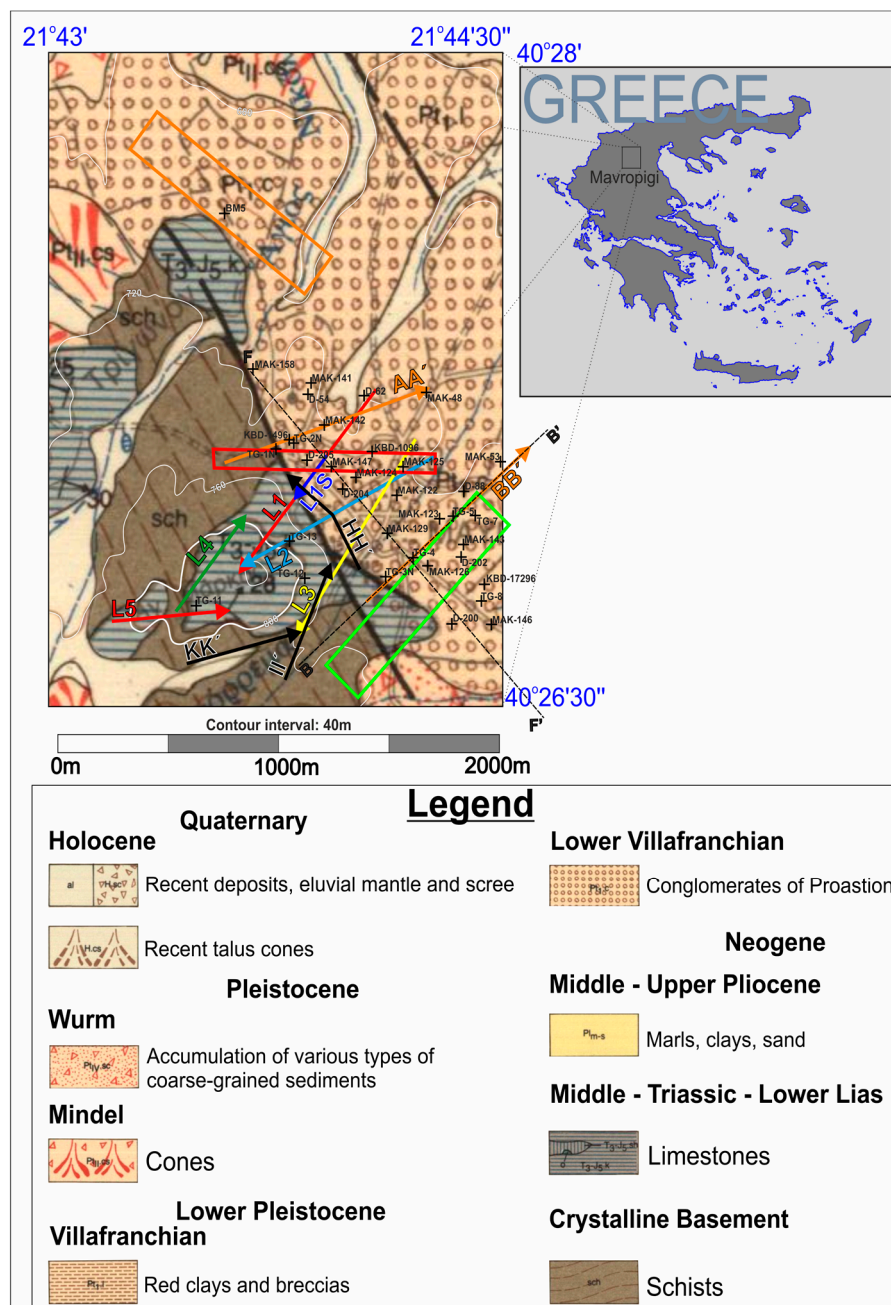

Figure 1. Geological map of the study area. Red and green rectangles correspond to north and south grids. Solid black, red, green, blue, and yellow arrows indicate the recent study lines, while the orange rectangle and arrows (AA', BB') correspond to a previous geophysical survey. The black dashed lines show the positions of the geological cross sections BB' and FF' presented in this study. The locations of boreholes are indicated with crosses.

The Greek Public Power Corporation applied an initial drilling program for delineating coal deposits (all but the TG boreholes in Figure 1). These boreholes usually did not reach the base of the pre-Neogene formations. As the excavations on the southern side of the Mavropigi open pit mine approach the edge of the Quaternary basin, stability issues of the final mine slopes have emerged. The geological information of the area was enriched with new geotechnical wells (BM5 &TG-1 to TG-13). The main target of this drilling program was to explore the depth and the dip of bedrock near the southern edge of the Mavropigi open pit mine. Two problems were revealed: (a) steep schist bedrock and (b) limestone bodies found over the schist bedrock. In addition, a 10–15 m thick tectonic contact zone was observed between the schist bedrock and the overlain limestone. This zone consists of completely weathered schist and/or limestone material. A typical geological section, which combines old and contemporary geological data, is shown in Figure 2.
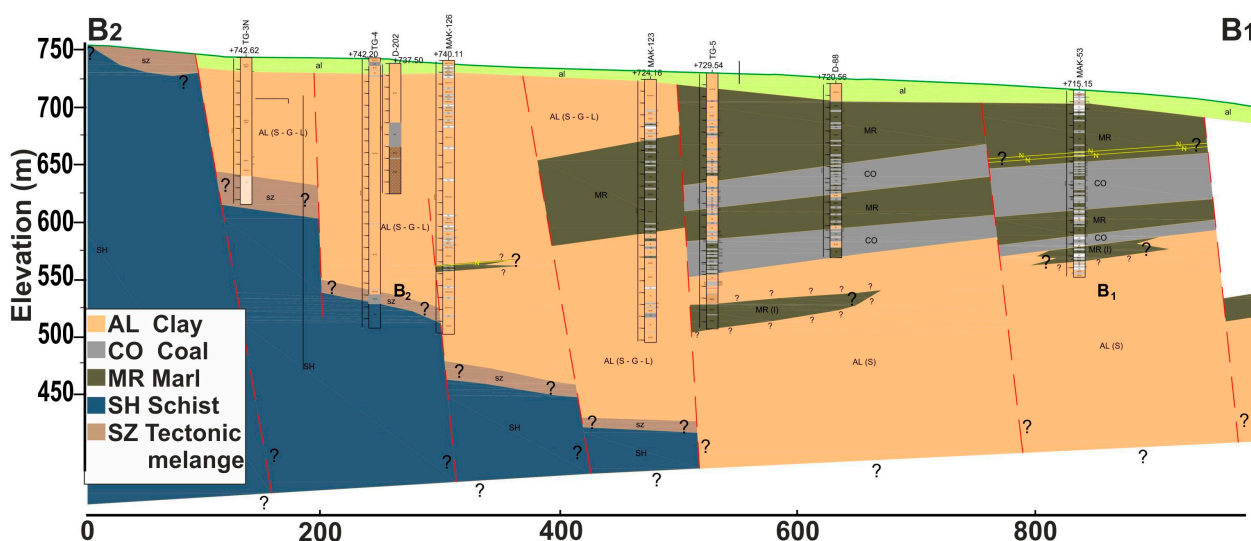

Figure 2. Typical geological section (B2-B1) along the ERT line BB', which is a portion of the corresponding geological section BB' (SW–NE).

Past geoelectrical surveys conducted north of the area under investigation included 2D and 3D ERT (orange rectangle and arrows AA' and BB' in Figure 1). One of the outcomes of this geophysical survey was a 3D resistivity data cube. This cube was generated through a process known as the 3D joint inversion (Figure 3) of the apparent resistivity data acquired from both Wenner–Schlumberger and dipole–dipole arrays on a grid along 12 tomography lines (orange rectangle in Figure 1).

The geophysical survey aimed to extract information mostly for the dip of the interface between schist bedrock and overlaying Neogene sediments and/or limestones. Electrical tomography was considered suitable for the investigation, since there is a good contrast between marls, schist, and limestone resistivity values. In the geophysical survey, dipole–dipole and gradient electrode arrays were utilized to detect both lateral and vertical resistivity variations, respectively. The site conditions, including differences in acoustic impedance and formation thickness, played a crucial role in the successful implementation of the seismic reflection method. The primary objective of the seismic reflection method was mainly focused on mapping the top of the schist bedrock.
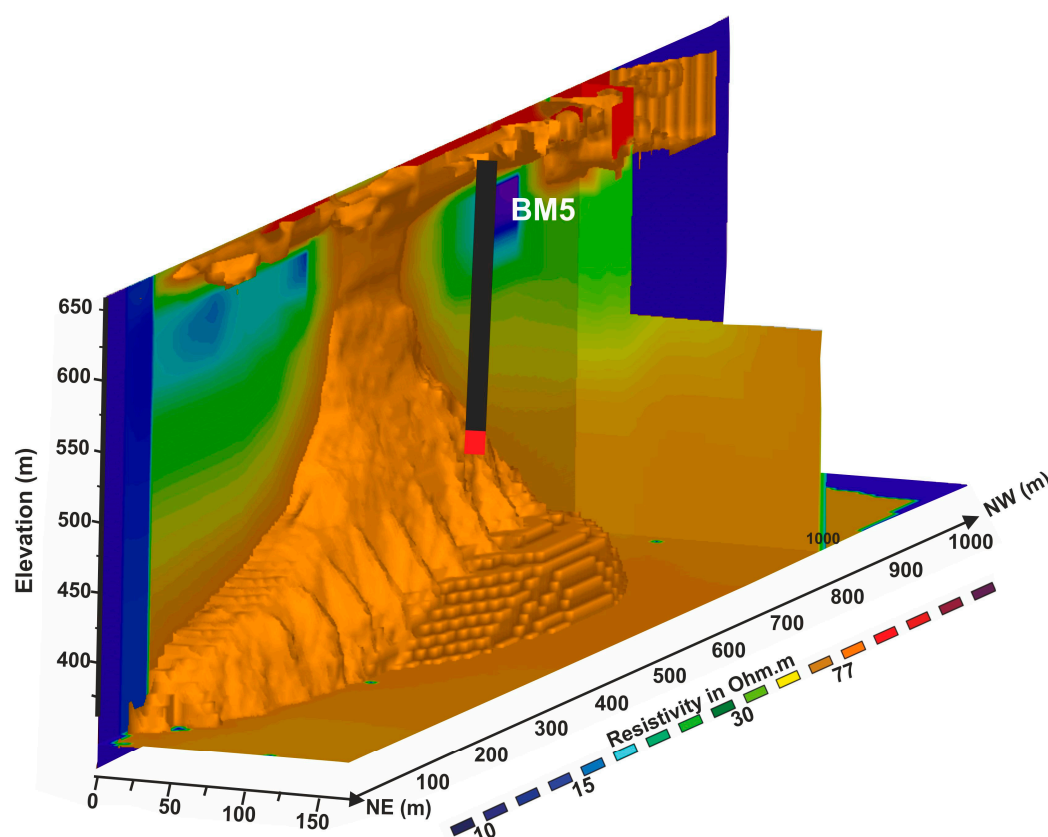
Figure 3. A view from the east–northeast of the 3D resistivity model. The contour of 77 Ohm · m (orange to red) delineates the top of the schist formation. Borehole BM5 is displayed in black and Quaternary, Neogene sediments, and Schist formation is in red.

3. Geophysical Methods

The electrical resistivity tomography (ERT) method has proven to be an extremely valuable tool in assessing slope stability, particularly in cases where traditional borehole investigations are unable to determine the lateral continuity of complex sliding surfaces [11,13,14]. The ERT method employed in this survey consisted of eight lines (L1–L5 and HH', II', and KK') and two grids (red and green rectangles), as shown in Figure 1. The grids consisted of a north grid (red, 1000 m × 80 m) and a south grid (green, 1000 m × 200 m), with line spacing of 20 and 40 m, respectively. In general, there is a good agreement between the geoelectrical sections for different arrays (dipole–dipole and gradient), with small discrepancies attributed mainly to varying lateral resolution. The robust (blocky) inversion was employed to enhance boundaries between the geoelectrical layers [38,39].

The seismic reflection method aimed at the mapping of the interface between the Neogene deposits and schist bedrock on the southern edge of the Mavropigi open pit mine. Geology, an important issue when applying the seismic reflection method, as raised from borehole data in the investigated area, fulfills a basic criterion for the successful application of this method. More specifically, the acoustic impedance contrast between Neogene sediments and bedrock formations is significant, meaning that this interface is a strong reflector.

To evaluate the efficiency of using the seismic reflection method and assess its capability to image the desired bedrock relief, simulations were conducted in a preliminary step. The purpose of these simulations was to replicate real conditions and determine the optimal survey configuration. In this process, a 2D seismic model of the region of interest was constructed using available geological data from existing boreholes and geological sections (Figure 2).

Based on the results from the simulations, seismic reflection data were acquired in the field over a portion of the geoelectrical line L1 (line L1S, Figure 1). The effectiveness of this method relies on the specific site conditions, such as variations in acoustic impedance and formation thickness, as well as the careful selection of acquisition parameters. To ensure optimal results, a "noise test" must be conducted [6,7]. Coherent noise such as airwaves, direct waves, and ground roll can obscure the reflected energy in seismic data. Data processing techniques have limited effectiveness in attenuating coherence noise; therefore, efforts primarily focus on minimizing its presence during data acquisition. The main, or conventional, processing steps for shallow seismic reflection data encompass various corrections and enhancements. These steps include elevation corrections for sources and receivers (static corrections), geometrical spreading corrections to recover the three-dimensional loss of seismic energy, deconvolution to improve temporal resolution, sorting traces in common midpoint gathers (CMPs), velocity analysis, dynamic (normal move out—NMO) correction, the stacking of the CMP gather traces after NMO correction, and the migration of the stacked section [7]. The static corrections require a velocity model often obtained from a seismic refraction experiment.

4. Results

4.1. Geoelectrical Survey

The past geoelectrical investigation pointed out that the bedrock relief displayed in Figure 3 exhibits very large dips [26]. According to the drilling data from borehole BM5 displayed in the same figure, the thickness of Neogene sediments (clay, marls, and lignite content) is 190 m. The schist bedrock depth, as it emerges from geoelectrical data, is in agreement with the above-mentioned borehole.

The geoelectrical survey primarily focuses on acquiring new data to enhance geological sections and contribute to geotechnical research. The specific objectives of this survey include the imaging of the top surface of the schists, delineating the contact zone between the Neogene or Triassic–Jurassic carbonates and the schist formation, identifying the presence of faults, and estimating the thickness of the limestone cover above the schist formation. In this geoelectrical survey, a total of eight electrical tomography lines were scanned, covering an approximate total length of 5700 m (Figure 1). For lines with a length of 1 km (L1, L2, and L3), the electrode spacing was set to 50 m. For lines with a length of 540 m (L4, L5, HH', II', and KK'), a smaller electrode spacing of 20 m was implemented.

From the geoelectrical sections along lines L1, L2, L3, L4, L5, and II' (Figures 4 and 5) and borehole information, the shallow high-resistivity zones (>150 Ohm·m) are attributed to the limestone body. The maximum thickness of this body does not exceed 50 m. A deeper geoelectrical thin zone with intermediate resistivity values (50–150 Ohm·m) is probably associated with the contact zone between the limestone and schist formations. This zone exhibits lower resistivity values compared to the ones from carbonates or schists due to increased moisture locally present within the fractured limestone and/or schist. Deeper high-resistivity values present in the southwest portion of sections L1, L2, and L3 are attributed to the schist bedrock, which is dipping to the northeast. Similarly, deeper high-resistivity values present in sections L4, L5, and KK' (Figure 5) are attributed to the schist bedrock. This schist layer is not present in section HH'(Figure 5).

According to Figure 6, the northeastern parts of sections L1, L2, L3, and HH' primarily consist of Quaternary and Neogene formations exhibiting resistivity values of less than 150 Ohm·m. These sediments are usually characterized by resistivity values less than 70 Ohm·m while, locally and near the surface they exhibit resistivity values between 70 and 150 Ohm·m (Figures 4–6).

According to Figure 7, in the north grid, the geoelectrical zone to the west is characterized by resistivity values greater than 150 Ohm·m. This higher resistivity zone is attributed to the bedrock, consisting of carbonates and schists, which dip to the southeast. The geoelectrical section obtained from the gradient array shows a distinct and prominent lower resistivity layer with a resistivity value of less than 150 Ohm·m. This layer is attributed

to the Quaternary and Neogene formations. A typical geoelectric section extracted from the resistivity data cube (Figure 8) indicates that the thickness of Neogene sediments is in agreement with the depth of the bedrock deduced from boreholes.
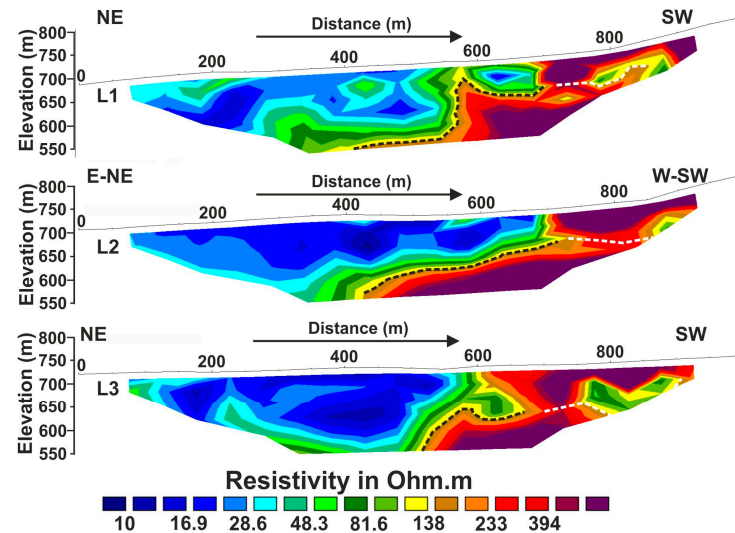

Figure 4. Geoelectrical sections (L1, L2, and L3) for gradient array. The black dotted line is attributed to the top of the schist bedrock and the white dotted line to the contact zone between the limestone and schist formations (tectonic contact).
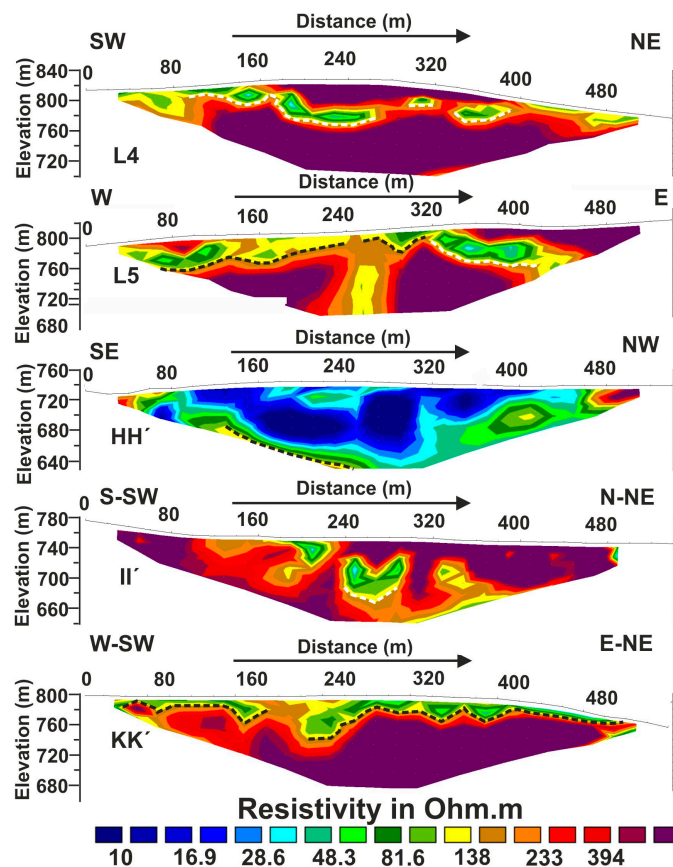

Figure 5. Geoelectrical sections (L4, L5, HH′, II′, and KK′) for gradient array. The black dotted lines correspond to the top of the schist bedrock and the white dotted lines are attributed to the contact zone between the limestone and schist formations (tectonic contact).
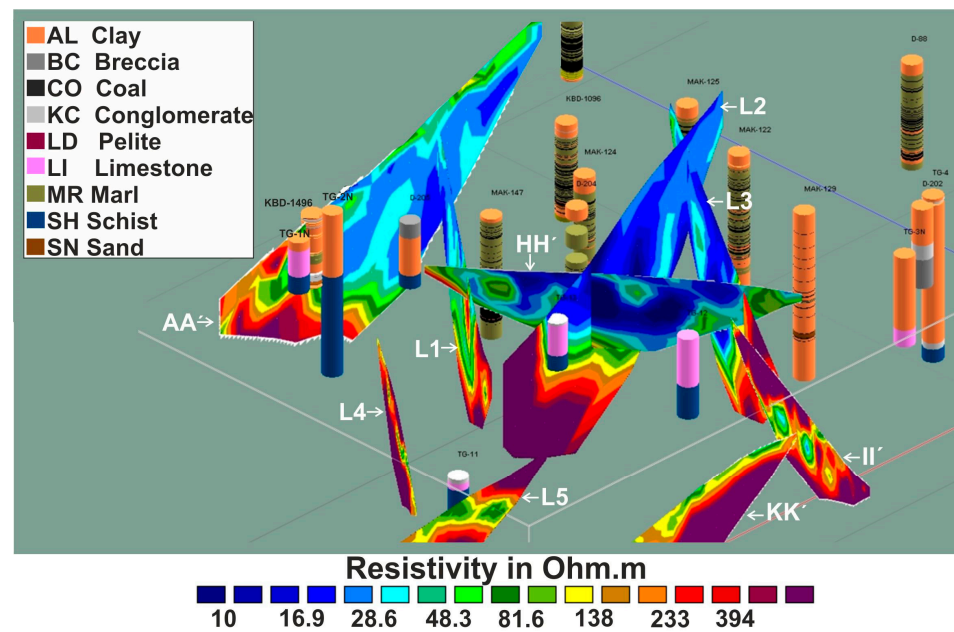
Figure 6. Fence diagram of selected geoelectrical sections (L1, L2, L3, L4, L5, AA', HH', II', and KK') for the dipole–dipole array. Lithology logs from boreholes at the survey area are shown as vertical cylinders, colored according to the legend at the upper left of image. View from the southwest.
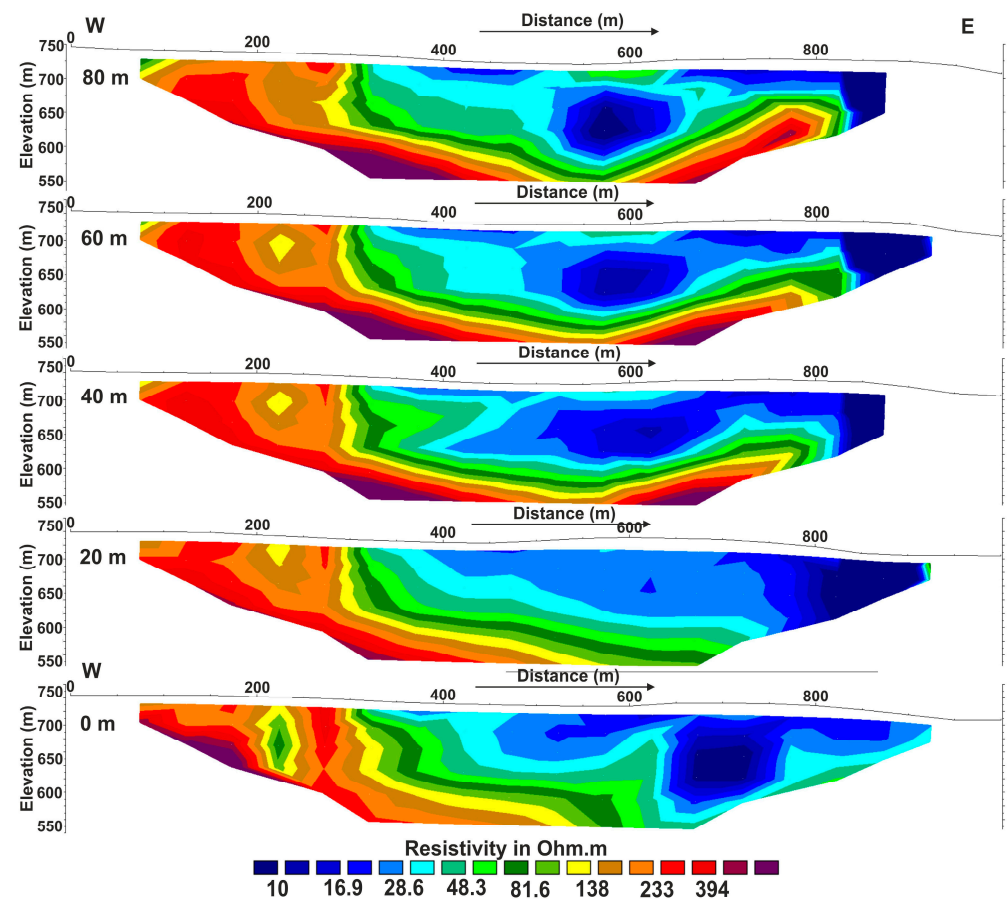

Figure 7. Geoelectrical sections from the north grid. The number in bold within each section indicates the line location on the grid. Line location increases northward.
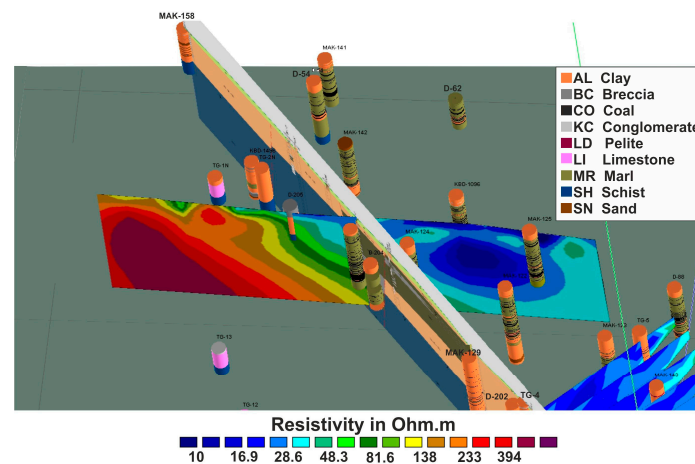
Figure 8. Geoelectrical section in the X–Z plane, located at 30 m in the Y direction, is extracted from the resistivity data cube, which is the outcome of the 3D joint inversion of apparent resistivity data (dipole–dipole—north grid). Lithology logs from boreholes at the survey area are shown as vertical cylinders, colored according to the legend at the upper right of image, the geology section FF', and parts of the ERT sections from the south grid (bottom right) are also displayed. View from the south.

Figure 9 displays 2D geoelectrical sections from the south grid where the maximum depth to bedrock (resistivity values higher than 150 Ohm·m) is approximately 400 m. Based on the combination of geological data (boreholes and geological section) and the two geoelectrical sections extracted from the 3D model (Figure 10), it is determined that the southwestern part of the south grid comprises schist and Triassic limestone formations.
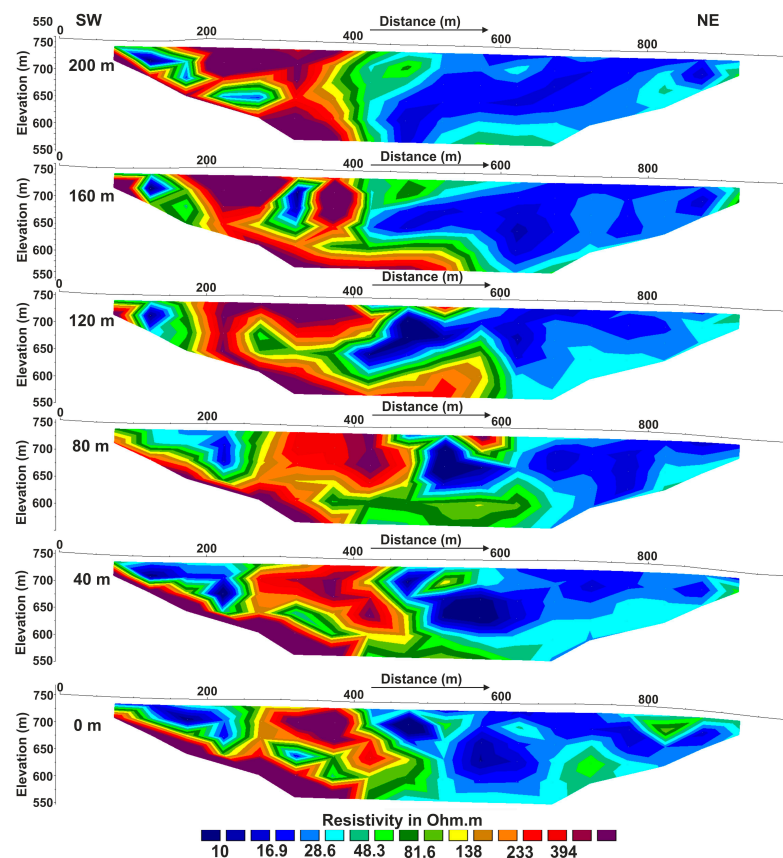

Figure 9. Geoelectrical sections from the south grid. The number in bold within each section indicates the line location on the grid. Line location increases northwestward.
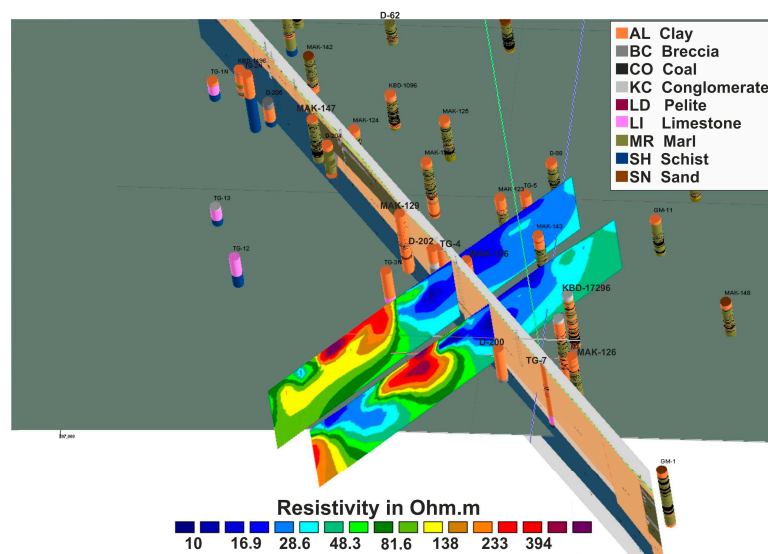
Figure 10. Geoelectrical sections in the X–Z plane, located at 20 and 180 m in the Y direction, are extracted from the resistivity data cube, which is the outcome of the 3D joint inversion of apparent resistivity data (dipole–dipole) of the south grid. Lithology logs from boreholes at the survey area are shown as vertical cylinders, colored according to the legend at the upper right of image and the geology section FF' are also displayed. View from the south.

4.2. Seismic Reflection

4.2.1. 2D P-SV Seismic Wave Simulation

Synthetic seismic data were generated using a 2D P-SV seismic simulator developed in the Applied Geophysics Lab of Technical University of Crete. The seismic velocity model was based on the geological section BB' and consists of three layers attributed to the following geological formations: (1) Neogene sentiments (marls), (2) lignite layers, and (3) the schist bedrock (Figures 2 and 11). Their P, S-velocity, and density values were set to: V_{p1} = 1750 m/s, V_{s1} = 437.5 m/s ρ_1 = 1.7 g/cm^3, V_{p2} = 1600 m/s, V_{s2} = 400 m/s ρ_2 = 1.3 g/cm^3, V_{p3} = 2800 m/s, and V_{s3} = 700 m/s, ρ_3 = 2.2 g/cm^3, respectively [40,41].
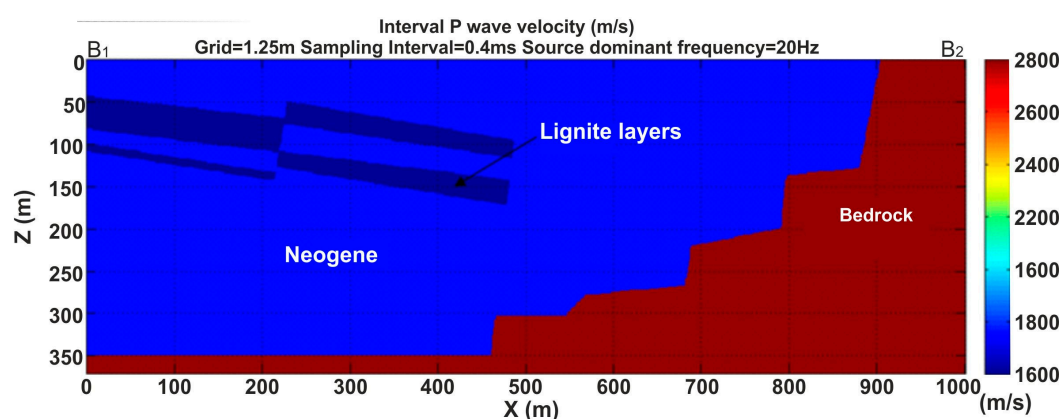

Figure 11. P wave velocity model (NE-SW), which corresponds to geological section B1–B2 (Figure 2).

The P-SV simulation employs a line seismic source and a predictor–corrector (MacCormack) finite difference scheme with second-order accuracy in time and fourth-order accuracy in space [42]. The first derivative of a Gaussian function with a fundamental frequency of 20 Hz was utilized as the time excitation of the line source, resulting, respectively, in 25 and 6 grid points per minimum P and S-wave wavelengths for a normal grid of 1.25 m. Boundary conditions ($\sigma_{xz} = \sigma_{zz} = 0$) were applied on the top edge of the model, while absorbing zones extend the remaining three model boundaries to suppress artificial backscattered waves from

the corresponding model edges. The simulation parameters are summarized in Table 1. An off-end shooting pattern was utilized with the source-first receiver offset equal to 95 m.

Table 1. Simulation parameters.

Synthetic Data			
Model length (m)	1000	Shot depth (m)	10
Model depth (m)	280	1st Shot X-coordinate (m)	5
Model grid (m)	1.25	Number of receivers (m)	72
Sampling interval (ms)	0.4	Receiver interval (m)	5
Record length (ms)	1200	Receiver depth (m)	0
Number of shots	55	1st Receiver X-coordinate (m)	100
Shot interval (m)	10	Nearest offset (m)	95

Figure 12 shows synthetic traces from a shot gather with the source at 5 m. A strong reflection from the Neogene sediments–bedrock interface is observed between 300 and 400 ms along the entire geophone spread. The nearest offset of 95 m was proved to be adequate for surface and reflected wave separation. Weak reflections from the top of lignite layers are present at near offset traces. The flowchart of Figure 13 summarizes the synthetic records of processing steps. The stack section (Figure 14) clearly displays the top of the bedrock reflector. However, this is not the case for the lignite bed reflectors. Additionally, diffractions are present mainly from the edges of the reflectors. After the application of finite difference migration [7], reflectors are placed at their correct position, while diffracted energy is concentrated at the edges of the reflectors. Comparing the migrated section with the velocity model, the bedrock reflector, as well as the reflectors of the lignite layers, are successfully imaged on the migrated section (Figure 15).
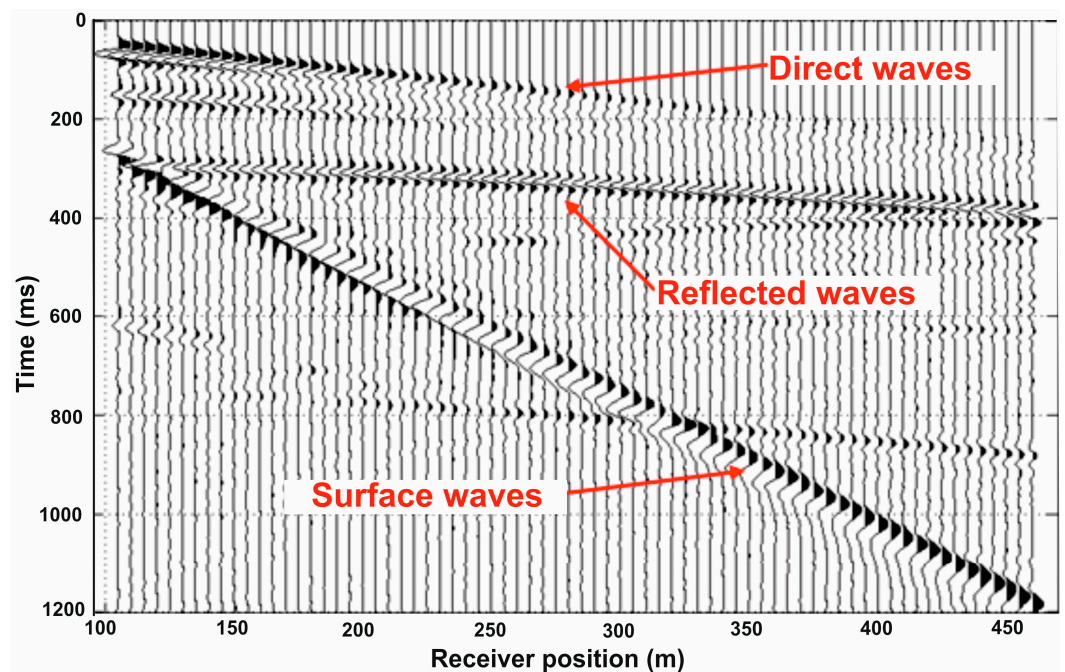

Figure 12. Shot gather from synthetic data for shot location at 5 m. Surface waves do not mask reflection from bedrock.
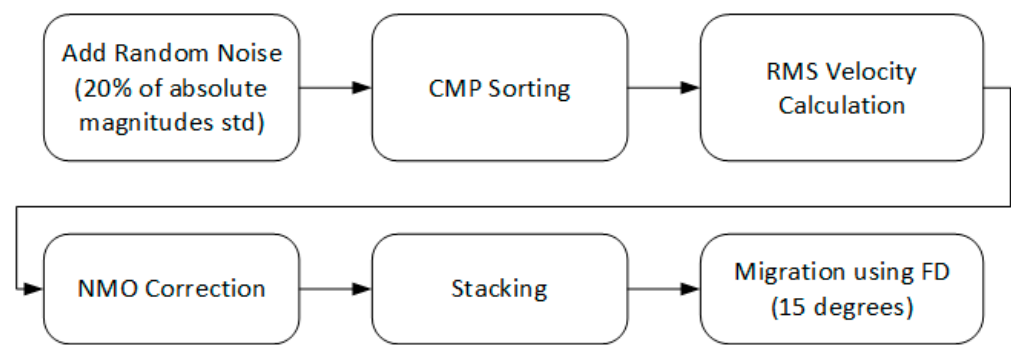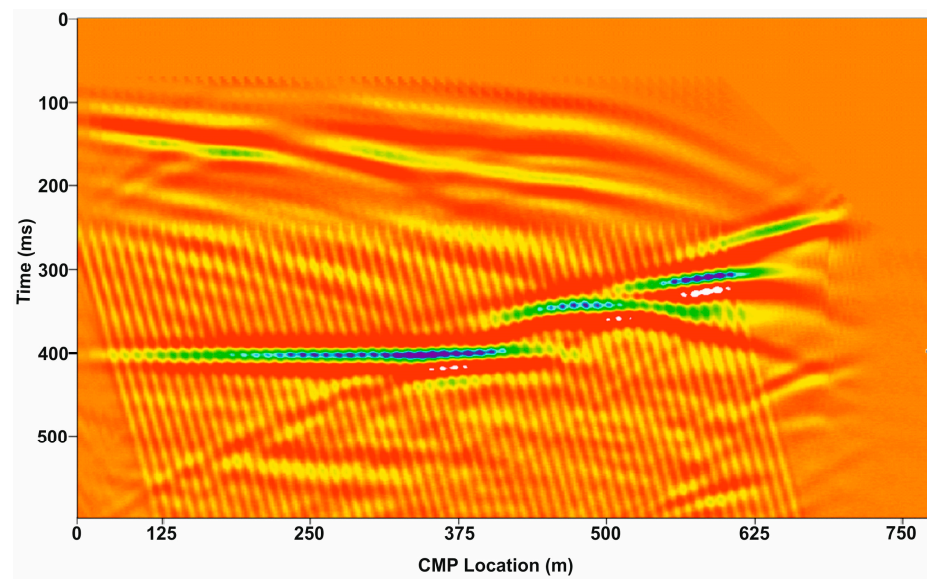
Figure 13. Synthetic data-processing flow.

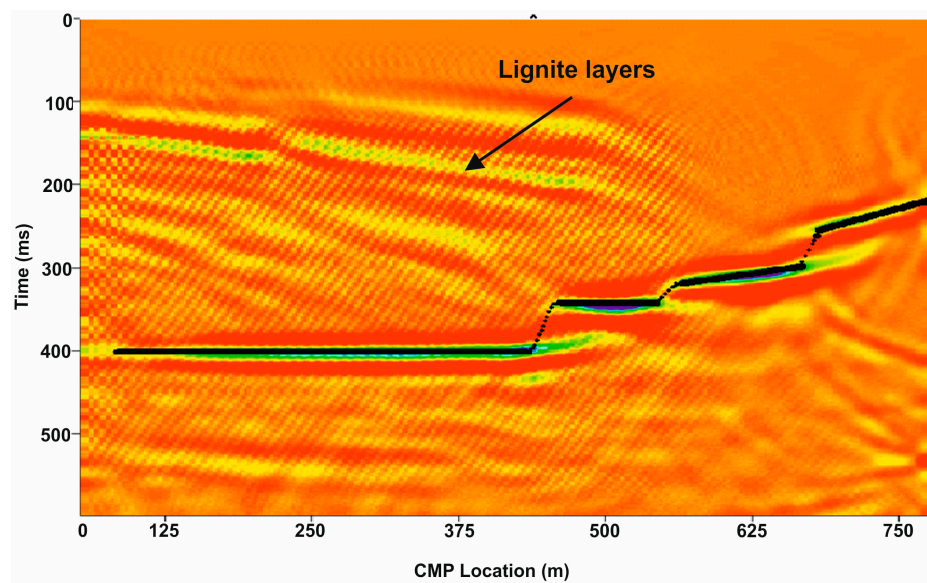**Figure 14.** Synthetic stack section along the line B1-B2 (NE–SW).

Figure 15. Synthetic migrated section along the line B1–B2 (NE–SW).

4.2.2. Field Experiment

After obtaining encouraging results from the simulations, the next step involved acquiring seismic reflection data in the field. The seismic reflection method focused on

scanning a portion (L1S) of the geoelectrical line L1, as shown in Figure 1. In the field, dynamite was utilized as the seismic source, which was placed in holes at depths greater than the thickness of the weathered layer. These holes were filled with sand to improve the coupling between the seismic source and the ground. The amount of dynamite was, in most cases, 4 kg. Noise test records (Figure 16) determined the optimum nearest offset.
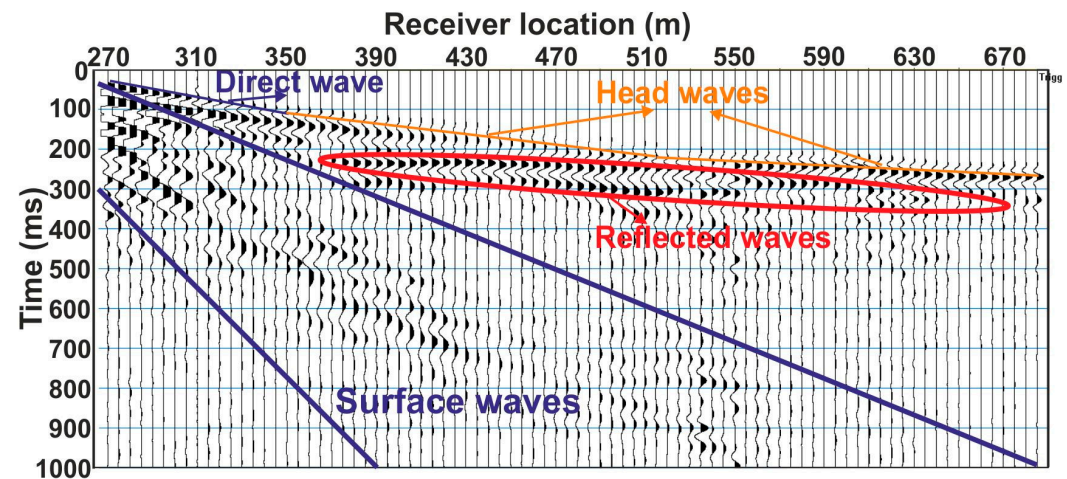

Figure 16. Shot gather from the noise test for the shot at 250 m. Coherent noise (surface waves) and reflected waves are indicated. The coherent noise masks a portion of the reflected waves. The number of receivers is 84.

An underground pipe carrying hot water from the electricity power station to the nearby city (Ptolemaida) for heating purposes crossed the seismic line at 415 m. To avoid causing damage to this pipe, the nearest shots were moved by 5 m (from 410 m and 420 m to 405 m and 425 m, respectively), and the amount of dynamite was reduced from 2 to 1 kg at the seven boreholes closest to the pipe. For the nearest shots (410 and 420 m), a fence of empty, shallow boreholes was drilled between the shot holes and the pipe in order to significantly attenuate the seismic energy, which travels directly from the explosives to the pipe.

A seismic refraction experiment was also carried out along line L1, using a hammer as a seismic source, in order to estimate the shallow seismic velocity model. This model (Figure 17) is employed for static corrections and setting the elevation datum at 700 m.
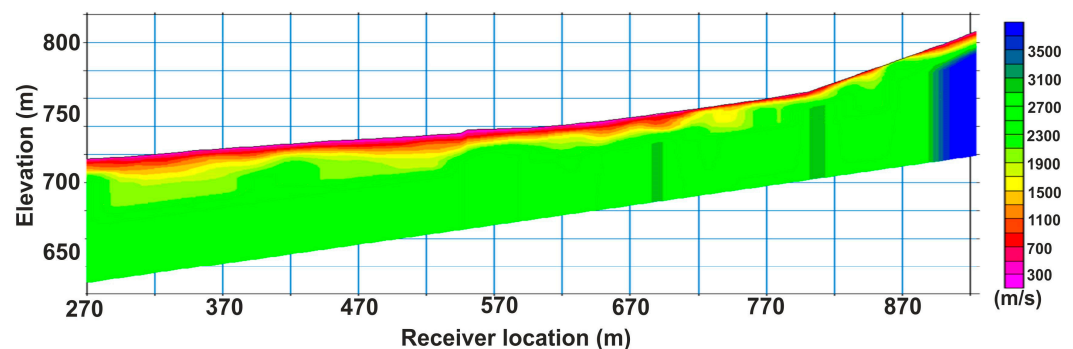

Figure 17. Shallow seismic velocity model for a portion of line L1, deduced from the seismic refraction experiment. The color scale corresponds to the P wave velocity.

Consequently, traces were sorted in CMPs (Figure 18a) followed by velocity analysis using semblance for the CMPs whose number of traces (fold) exceeded 11. For the NMO correction in CMP gathers (Figure 18b), the root mean square (RMS) velocity model, shown in Figure 19, was employed. The processing workflow is displayed in Figure 20. The spectral balancing technique applied on the stack section recovered the amplitudes of the

seismic trace and increased the dominant frequency from 20 to 30 Hz [43] (Figure 21a). The depth section is the outcome of post-stack explicit finite difference depth migration [44] (Figure 21b). In the migrated section, the reflectors are placed shallower with higher dips. In Figure 22, the depth-migrated section and borehole D-205 were superimposed on the corresponding portion of the ERT section (dipole–dipole array) from Line 1. This borehole is off the line at a 58 m distance from L1, and its projection intersects Line L1 at 430 m (Figure 1). From the migrated section, a normal fault is present, which (according to the ERT section) exceeds 100 m. From the comparison of electrical tomography and seismic sections, we observe an acceptable fit regarding the fault. The seismic section provides more accurate information about the inclination of the fault. This fault appears from 450 m until the end of the seismic section, and its inclination is approximately 45 degrees.
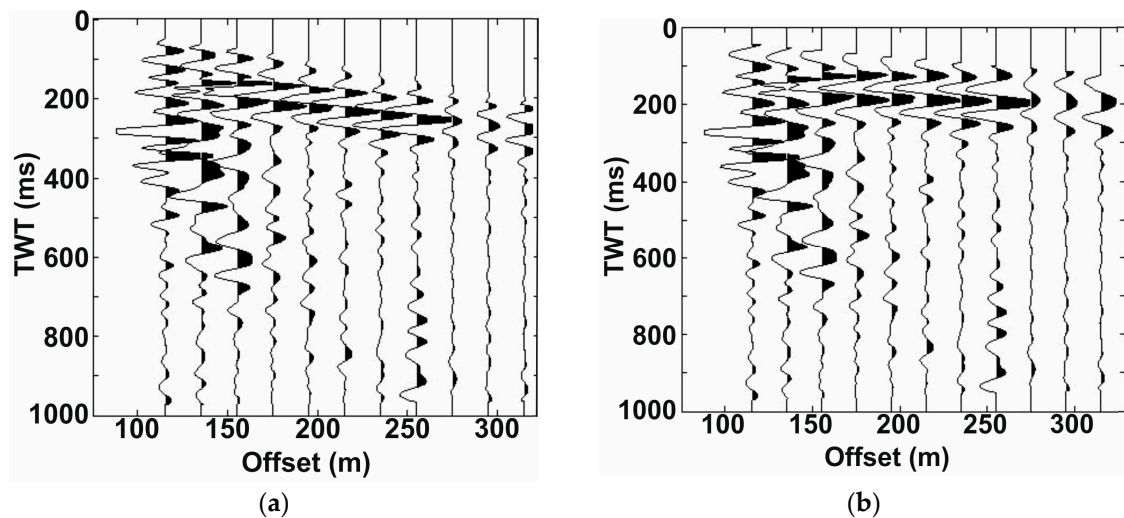

(a)   (b)

Figure 18. CMP gather at 465 m before (**a**) and after (**b**) NMO correction.
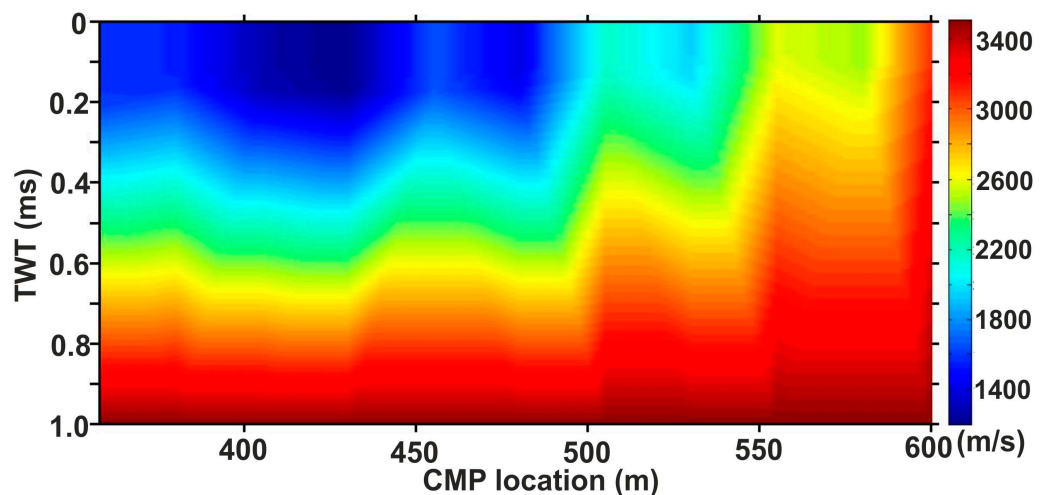

Figure 19. Real data. Root mean square (RMS) velocity model deduced from the velocity analysis of CMP gathers.
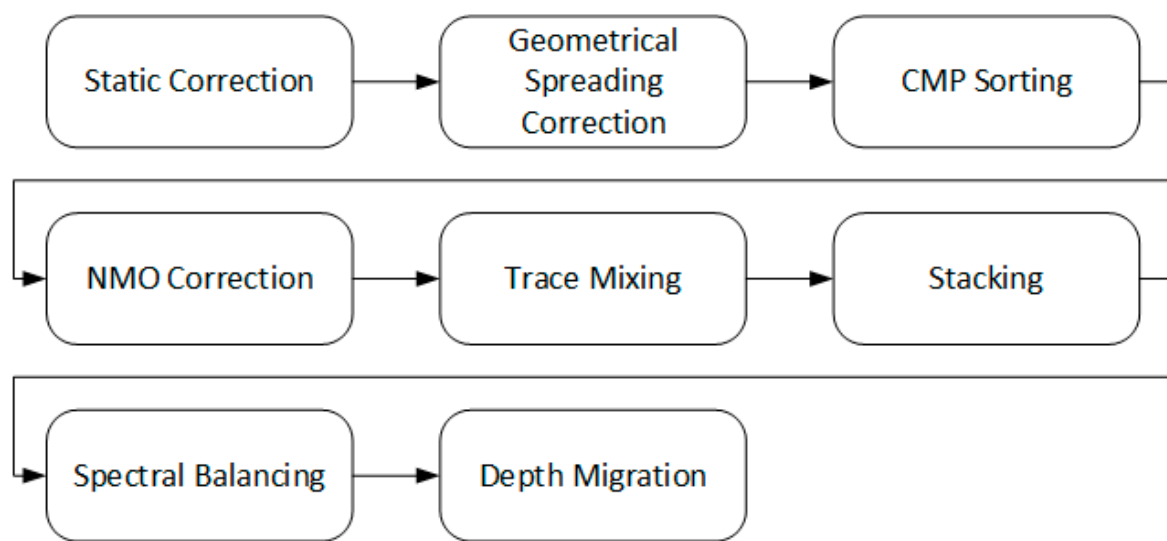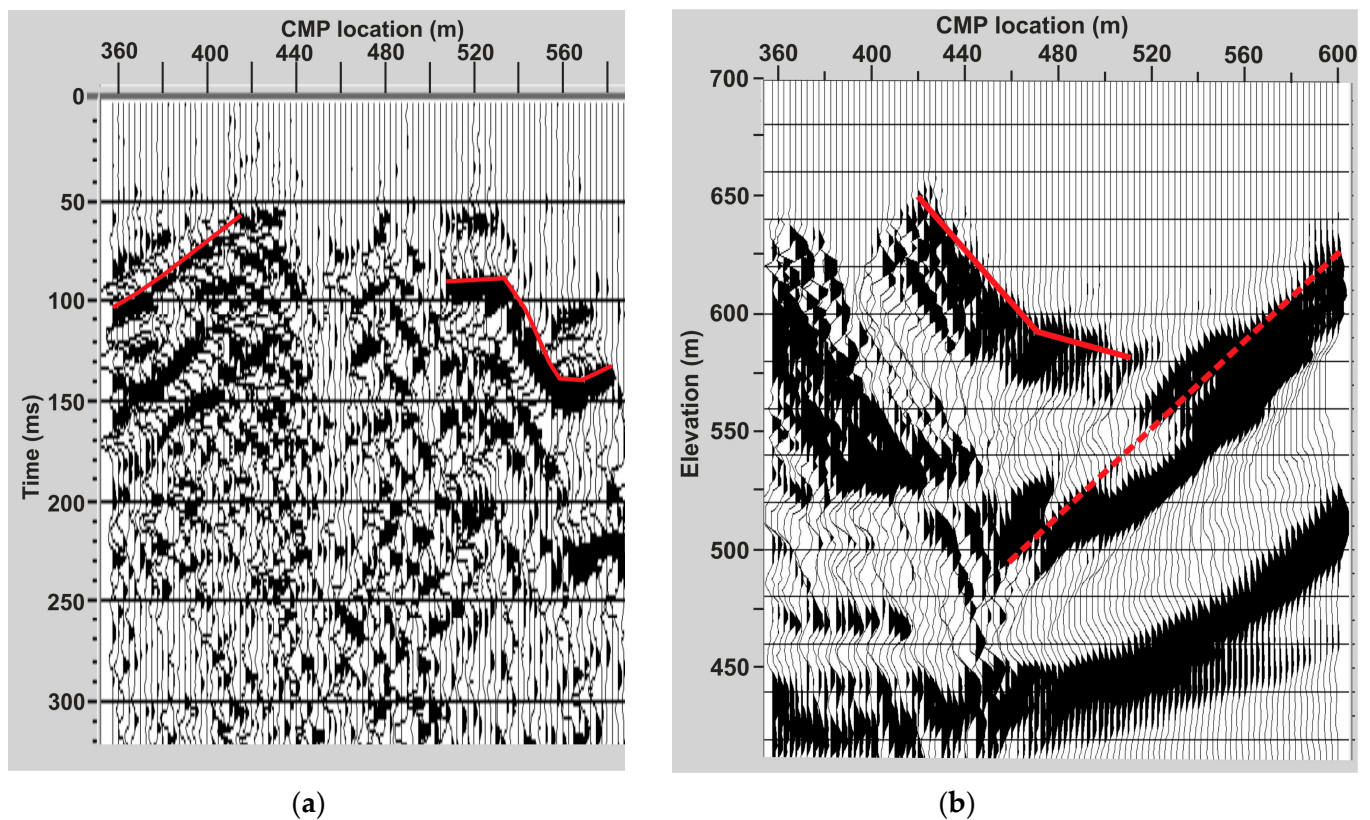
Figure 20. Processing flow of real data.

Figure 21. (**a**) Stack section. (**b**) Depth-migrated section. The red lines correspond to the schist bedrock and the red dashed line indicates a fault.
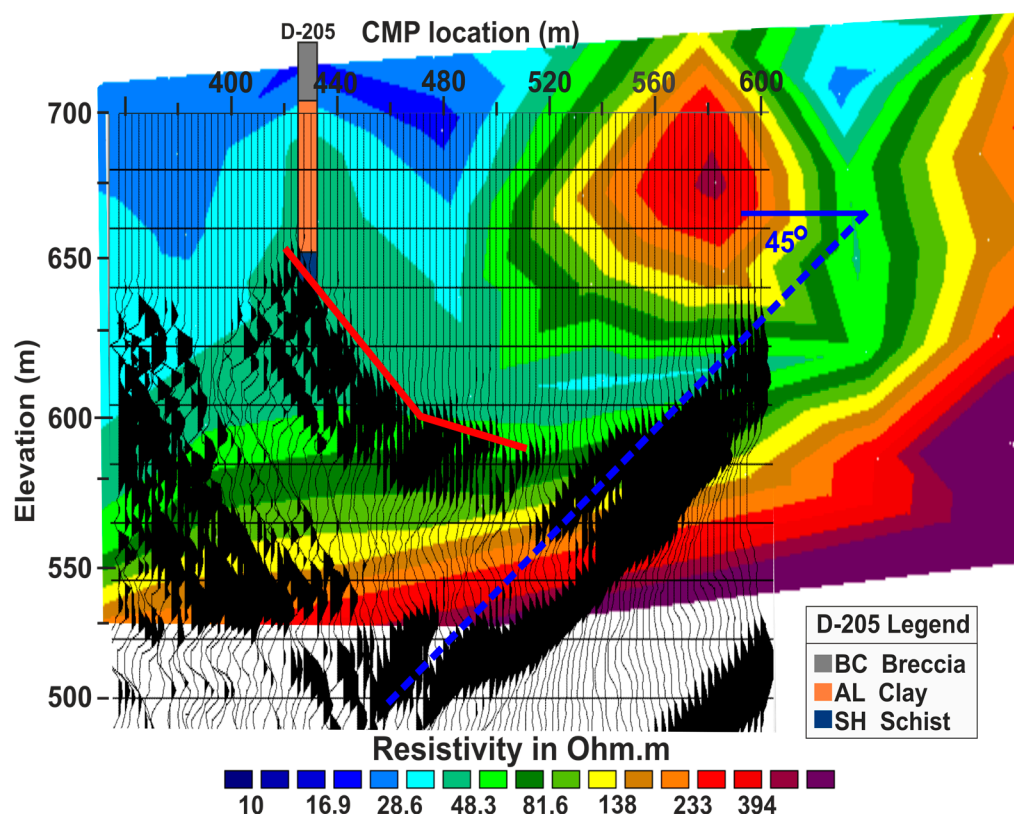
Figure 22. Superposition of depth-migrated section on ERT Line 1 (dipole–dipole array). Red line corresponds to the schist bedrock and blue dashed line indicates a fault with a dip of 45 degrees.

5. Discussion

The integration of seismic and electrical methods proved sufficient for mapping the carbonates and schist tectonic contact at the Mavropigi open pit mine. The present work provides the geophysical results related to the sustainability of lands with the scope to avoid their misuse and to increase geotechnical safety [1,3].

It is shown that the combination of geophysical techniques sensitive to different physical properties can reveal subsurface structures like tectonic contacts, which is not always the case when using the classic engineering geological methods [1]. The seismic reflection method proved useful for a shallow depth of investigation [2–5]. Based on the fact that the vertical resolution of electrical methods is lower than the one of seismic reflection, the tectonic contacts are better imaged on the seismic section.

Gradient and dipole–dipole arrays for the 2D ERT survey achieve good vertical and lateral resolution and distinguish the limestone body overlaying the schist bedrock [35]. The tectonic contact zone between limestone and schist formations was properly imaged. Quaternary and Neogene formations are attributed to resistivity values less than 150 Ohm·m. According to the geoelectrical sections L1, L2, and L3 (Figure 4), the schist bedrock is dipping to the northeast. A good agreement exists between geoelectrical and geological data (boreholes and geological sections) from the survey area.

Seismic wave propagation simulations played a crucial role in verifying the effectiveness of the seismic reflection method and provided valuable information regarding the optimal geometry and recording parameters for the acquisition of seismic reflection data. Additionally, a noise test was conducted to ensure that the acquired seismic reflection data were not affected by significant coherent noise that could interfere with the target reflectors [6]. The outcome of the seismic reflection data processing was the depth section that accurately delineated the interface between the Neogene sediments and the schist bedrock [7,27,43]. This depth section also revealed the presence of an NE-dipping fault,

highlighting its location and extent within the subsurface. This fault interrupts the bedrock continuation. The seismic section provides a more detailed image of this feature compared to the corresponding ERT section (Figure 22). Differences appeared between the seismic section and the geoelectrical section L1 regarding the depth and the shape of the top of the bedrock. More specifically, the Neogene sediments and bedrock interface is dipping to the SW. According to the geoelectrical section L1, the top of the bedrock present at horizontal distances between 400 and 580 m is flat. A possible explanation is that both the horizontal and vertical resolution of the ERT section at the depth of interest is controlled by the 50 m electrode spacing.

The geophysical survey in an open pit mine area ensured objectives that are closely connected with sustainability, not only during the exploitation stage, but also in the future reclamation process. These objectives include, among others, the optimization of productivity, cost savings, and zero accidents [1,34].

6. Conclusions

A geophysical study carried out next to the Mavropigi open pit lignite mine provides slope instability, landslide, and limestone body movement tracking for the geotechnical safety planning of the mine expansion and provides information for future rehabilitation.

The integration of a shallow seismic reflection and the ERT method led to the carbonate and schist tectonic contact mapping in three dimensions and fault imaging, as well as the delineation of the Neogene to Schist/Carbonates formation contact, which is the main surface of future landslides. This geophysical investigation proved very useful for studies related to the assessment of stability for geotechnical safety during excavations as well as for land reclamation planning in the immediate future.

Author Contributions: Conceptualization, N.A. and A.V.; Methodology, N.A., A.V., G.K. and N.E.; Software, N.A., A.V., G.K. and N.E.; Interpretation, N.A., A.V., G.K., Z.A., C.S. and N.E.; Investigation, H.H., Z.A. and C.S.; Writing—original draft preparation, N.A., A.V. and G.K.; Writing—review and editing, N.A., Z.A., N.E. and A.V.; Supervision, A.V. All authors have read and agreed to the published version of the manuscript.

Institutional Review Board Statement: Not applicable.

Informed Consent Statement: Not applicable.

Data Availability Statement: The data presented in this study are available upon reasonable request from the corresponding author.

Conflicts of Interest: The authors declare no conflict of interest.

References

1. Burlutsky, S.B. Geophysical surveys as a tool for geotechnical monitoring of disturbed land reclamation. In *IOP Conference Series: Earth and Environmental Science*; IOP Publishing: Bristol, UK, 2022; Volume 1070. [CrossRef]
2. Greenhalgh, S.; Suprajitno, M.; King, D. Shallow seismic reflection investigations of coal in the Sydney basin. *Geophysics* **1986**, *51*, 1426–1437. [CrossRef]
3. Miller, R.D.; Saenz, V.; Huggins, R.J. Feasibility of CDP seismic reflection to image structures in a 220-m deep, 3-m thick coal zone near Palau, Coahuila, Mexico. *Geophysics* **1992**, *57*, 1373–1381. [CrossRef]
4. Baker, G.S. *Processing Near-Surface Seismic Reflection Data A Primer*; Course Notes Series No. 9; Society of Exploration Geophysicists: Houston, TX, USA, 1999; p. 79.
5. Diogo, L.; Diagon, F.; Prado, R. Bedrock imaging using post-critical shallow seismic reflection data. *J. Appl. Geophys.* **2004**, *57*, 1–9. [CrossRef]

6.   Sheriff, R.E.; Geldart, L.P. *Exploration Seismology: History, Theory, and Data Acquisition*; Cambridge University Press: Cambridge, UK, 1995.

7.   Yilmaz, O. *Seismic Data Processing: Society of Exploration Geophysics*; SEG: Houston, TX, USA, 1987.

8.   Onyebueke, E.O.; Manzi, M.S.D.; Durrheim, R.J. High-resolution shallow reflection seismic integrated with other geophysical methods for hydrogeological prospecting in the Nylsvley Nature Reserve, South Africa. *J. Geophys. Eng.* **2018**, *15*, 2658–2673. [CrossRef]

9.   Dehghannejad, M.; Malehmir, A.; Svensson, M.; Lindén, M.; Möller, H. High-resolution reflection seismic imaging for the planning of a double-train-track tunnel in the city of Varberg, southwest Sweden. *Near Surf. Geophys.* **2017**, *15*, 226–240. [CrossRef]

10.   Yilmaz, O. *Engineering Seismology with Applications to Geotechnical Engineering*; Tulsa, O.K., Ed.; Society of Exploration Geophysicists: Houston, TX, USA, 2015.

11.   Drahor, M.; Gokturkler, G.; Berge, M.; Kurtulmus, T. Application of electrical resistivity tomography technique for investigation of landslides: A case study from turkey. *Environ. Geol.* **2006**, *50*, 147–155. [CrossRef]

12.   Perrone, A.; Vassallo, R.; Lapenna, V.; Di Maio, C. Pore water pressures and slope stability: A jointed geophysical and geotechnical analysis of a landslide. *J. Geophys. Eng.* **2008**, *5*, 323–337. [CrossRef]

13.   Colangelo, G.; Lapenna, V.; Loperte, A.S.; Perrone, A.; Telesca, L. 2D electrical resistivity tomographies for investigation recent activation landslides in Basilicate region (Southern Italy). *Ann. Geophys.* **2008**, *51*, 275–285.

14.   Chambers, J.; Meldrum, P.; Gunn, D.; Wilkinson, P.; Kuras, O.; Weller, A.; Ogilvy, R. Hydrogeophysical monitoring of landslide processes using automated time-lapse electrical resistivity tomography (ALERT). In Proceedings of the 15th European Meeting of Environmental and Engineering Geophysics 2009, Dublin, Ireland, 3–5 September 2009.

15.   Apostolopoulos, G.; Antoniades, C.; Pavlopoulos, K. The electrical resistivity method—A useful tool in evaluating geological and geotechnical conditions for constructing and engineering projects. In Proceedings of the 6th Balkan Geophysical Society 2011, Budapest, Hungary, 3–6 October 2011.

16.   Yilmaz, S. A case study of the application of electrical resistivity imaging for investigation of a landslide along the highway. *Int. J. Phys. Sci.* **2011**, *6*, 5843–5849.

17.   Andronikidis, N.; Kritikakis, G.S.; Agioutantis, Z.; Vafidis, A.; Steiakakis, C.; Papageorgiou, C.; Schilizzi, P.; Tsourlos, P.; Vargemezis, G. Mapping the Bedrock Using ERT for Slope Stability Studies at Mavropigi Lignite Open Pit Mine, Northern Greece. In Proceedings of the 8th Balkan Geophysical Society 2015, Chania, Greece, 5–8 October 2015.

18.   Bryson, S. Evaluation of geotechnical parameters using electrical Resistivity Measurements. In Proceedings of the Geo-Frontiers 2005, Austin, TX, USA, 24–26 January 2005.

19.   Oh, S.; Sun, C. Combined analysis of electrical resistivity and geotechnical SPT blow counts for the safety assessment of fill dam. *Environ. Geol.* **2008**, *54*, 31–42. [CrossRef]

20.   Siddiqui, F.; Osman, S. Integrated Geo-Electrical and geotechnical data for soil characterization. *Int. J. Appl. Phys. Math* **2012**, *2*, 104–106. [CrossRef]

21.   Siddiqui, F.; Osman, S. Electrical resistivity based nondestructive testing method for determination of soil's strength properties. *Adv. Mater. Res.* **2012**, *488–489*, 1553–1557. [CrossRef]

22.   Sastry, R.; Mondal, S.; Pachauri, A. 2D Electrical resistivity tomography of a Landslide in Garhwal Himalaya. In Proceedings of the 6th International Conference and Exposition on Petroleum 2006, Kolkata, India, 9–11 January 2006.

23.   Perrone, A.; Piscitelli, S.; Lapenna, V.; Loperte, A.; Di Maio, C.; Vassallo, R. Electrical resistivity tomography and geotechnical techniques for the stability analysis of the Tricario Landslide. In Proceedings of the 13th European Meeting of Environmentaland Engineering Geophysics 2007, Istanbul, Turkey, 3–5 September 2007.

24.   Soupios, P.; Georgakopoulos, P.; Papadopoulos, N.; Andreadakis, A.; Vallianatos, F.; Sarris, A.; Makris, J.P. Use of engineering geophysics to investigate a site for a building foundation. *J. Geophys. Eng.* **2007**, *4*, 94–103. [CrossRef]

25.   Chavez, R.; Tejero, A.; Aguilar, D. A 3D Electrical Resistivity Tomography Carried Out to Characterize the Subsoil (Fractures and Subsidence) Beneath a Reside. Extended abstracts, Near Surface Geoscience 2012. In Proceedings of the 18th European Meeting of Environment and Engineering Geophysics, Paris, France, 3–5 September 2012.

26.   Hamdan, H.; Andronikidis, N.; Kritikakis, G.; Economou, N.; Agioutantis, Z.; Schilizzi, P.; Steiakakis, C.; Papageorgiou, C.; Tsourlos, T.; Vargemezis, G.; et al. Contribution of electrical tomography methods in geotechnical investigations at Mavropigi lignite open pit mine, Northern Greece. *Environ. Earth Sci.* **2014**, *72*, 1589–1598. [CrossRef]

27.   Economou, N.; Kritikakis, G.; Manoutsoglou, E.; Vafidis, A. Fast and efficient void detection in carbonates by combined ERT and borehole data: A case study from Chania Airport in Greece. *Lead. Edge* **2022**, *41*, 322–330. [CrossRef]

28.   Chambers, J.E.; Ogilvy, R.D.; Kuras, O.; Cripps, J.C.; Meldrum, P.I. 3D electrical mapping of known targets at controlled environmental test site. *Environ. Geol.* **2002**, *41*, 690–704. [CrossRef]

29.   Bentley, L.R.; Gharibi, M. Two and three-dimensional electrical resistivity imaging at a heterogeneous site. *Geophysics* **2004**, *69*, 674–680. [CrossRef]

30.   Tsourlos, P. Inversion of electrical resistivity tomography data deriving from 3D structures. *Bull. Hell. Geol. Soc.* **2004**, *36*, 1289–1297. [CrossRef]

31.   Papadopoulos, N.; Tsourlos, P.; Tsokas, G.; Sarris, A. Two dimensional and Three-dimensional Resistivity Imaging in Archaeological Site Investigation. *Archaeol. Prospect.* **2006**, *13*, 163–181. [CrossRef]

32. Dahlin, T.; Loke, M. Quasi-3D resistivity imaging: Mapping of three dimensional structures using two dimensional DC resistivity techniques. In Proceedings of the 3rd Meeting Environmental and Engineering Geophysics, Aarhus, Denmark, 8–11 September 1997.

33. Aizebeokhai, A.P.; Olayinka, A.I.; Singh, V.S. Numerical evaluation of 3D geoelectrical resistivity imaging for environmental and engineering investigations using orthogonal 2D profiles. *SEG Expand. Abstr.* **2009**, *28*, 1440–1444. [CrossRef]

34. Aizebeokhai, A. 2D and 3D geoelectrical resistivity imaging: Theory and field design. *Sci. Res. Essays.* **2010**, *5*, 3592–3605.

35. Loke, M.; Barker, R. Practical techniques for 3D resistivity surveys and data inversion. *Geophys. Prospect.* **1996**, *44*, 499–523. [CrossRef]

36. Loke, M.; Barker, R. Rapid least-squares inversion of apparent resistivity pseudosections using a quasi-Newton method. *Geophys. Prospect.* **1996**, *44*, 131–152. [CrossRef]

37. Metaxas, A.; Karageorgiou, D.; Varvarousis, G.; Kotis, T.; Ploumidis, M.; Papanikolaou, G. Geological evolution-stratigraphy of Florina, Ptolemaida, Kozani and Saradaporo graben. *Bull. Geol. Soc. Greece* **2006**, *40*, 161–172. [CrossRef]

38. Claebout, J.; Muir, F. Robust modeling with erratic data. *Geophysics* **1973**, *38*, 826–844. [CrossRef]

39. Ellis, R.; Oldenburg, D. Applied geophysical inversion. *Geophys. J. Int.* **1994**, *116*, 5–11. [CrossRef]

40. Brokesova, J.; Zahradnik, J.; Paraskevopoulos, P. Ray and finite-difference modelling of CDP seismic sections for shallow lignite deposits. *J. Appl. Geophys.* **2000**, *45*, 261–272. [CrossRef]

41. Tselentis, G.; Paraskevopoulos, P. Application of a high-resolution seismic investigation in a Greek coal mine. *Geophysics* **2002**, *67*, 50–59. [CrossRef]

42. Vafidis, A.; Abramovici, F.; Kanasewich, E.R. Elastic wave propagation using fully vectorized high order finite differences. *Geophysics* **1992**, *57*, 218–232. [CrossRef]

43. Stockwell, R.G.L.; Mansinha, L.R.P.; Lowe, R.P. Localization of the complex spectrum: The S transform. *IEEE Trans Signal Process.* **1996**, *44*, 998–1001. [CrossRef]

44. Soubaras, R. Explicit 3D migration using equiripple polynomial expansion and Laplacian synthesis 1992. In *SEG Technical Program Expanded Abstracts 1992*; Society of Exploration Geophysicists: Houston, TX, USA, 1992; pp. 905–908.